

Sensor Fusion and Resource Management in MIMO-OFDM Joint Sensing and Communication

Elia Favarelli, *Member, IEEE*, Elisabetta Matricardi, *Student Member, IEEE*, Lorenzo Pucci, *Student Member, IEEE*, Wen Xu, *Senior Member, IEEE*, Enrico Paolini, *Senior Member, IEEE*, and Andrea Giorgetti, *Senior Member, IEEE*

Abstract—This study explores the promising potential of integrating sensing capabilities into multiple-input multiple-output (MIMO)-orthogonal frequency division multiplexing (OFDM)-based networks through innovative multi-sensor fusion techniques, tracking algorithms, and resource management. A novel data fusion technique is proposed within the MIMO-OFDM system, which promotes cooperative sensing among monostatic joint sensing and communication (JSC) base stations by sharing range-angle maps with a central fusion center. To manage data sharing and control network overhead introduced by cooperation, an excision filter is introduced at each base station. After data fusion, the framework employs a three-step clustering procedure combined with a tracking algorithm to effectively handle point-like and extended targets. Delving into the sensing/communication trade-off, resources such as transmit power, frequency, and time are varied, providing valuable insights into their impact on the overall system performance. Additionally, a sophisticated channel model is proposed, accounting for complex urban propagation scenarios and addressing multipath effects and multiple reflection points for extended targets like vehicles. Evaluation metrics, including optimal sub-pattern assignment (OSPA), downlink sum rate, and bit rate, offer a comprehensive assessment of the system’s localization and communication capabilities, as well as network overhead.

Index Terms—Joint sensing and communication, tracking, OFDM, probability hypothesis density filter, multi-Bernoulli mixture filter, resource allocation, data fusion.

I. INTRODUCTION

THE prominence of safety in urban environments has recently emerged as a critical area of interest. This requires the integration of advanced sensing technologies. The growing interest in sensing stems from its potential to enable several applications, including but not limited to, traffic monitoring, autonomous driving, and environmental mapping. These applications are poised to benefit greatly from effectively utilizing radio frequency signals for sensing purposes [1]. Of particular importance is the advancement in sensing

capabilities facilitated by the transition to higher frequency bands and the use of larger antenna arrays [2], [3]. This trend seems to perfectly capture the vision of the next generation of mobile networks, which are expected to encompass a wide range of novel capabilities and services, among which sensing seems one of the most prominent.

The sharp increase in the number of base stations (BSs) opens the door to the development of precise and reliable localization systems [4], [5]. This, in turn, paves the way for enhanced safety measures in urban settings [6]. Additionally, the advent of massive MIMO technology at millimeter-wave (mmWave) frequencies offers the opportunity not only to achieve remarkable data transmission rates but also to attain accurate object position estimation [7]. This noteworthy capability is anticipated to address emerging communication challenges effectively, embracing crucial aspects such as precise beam management [8], accurate estimation of target direction for beam tracking to maintain high-quality links [9], and the application of predictive beam tracking using JSC in vehicular scenarios [10].

Moreover, as we delve into the potential of 6G mobile radio networks and their applications, it is essential to examine the existing gaps in research. While significant strides have been made in integrating sensing and communication capabilities, certain aspects remain underexplored. In particular, the exploitation of mobile radio networks as an enabler for distributed and cooperative sensing is still underinvestigated. Along these lines, the benefits of cooperation, as well as its impact on network overhead, have not been thoroughly addressed. Furthermore, the remarkable flexibility offered by mobile networks to allocate resources based on user needs has not been fully exploited for sensing, hindering adjustment of the sensing/communication trade-off to specific requirements [11]–[13]. The integration of cooperative sensing into the mobile network framework stands as an unexplored frontier, promising to enhance both the efficiency of sensing applications and the overall performance of the network.

This study explores the feasibility of enabling sensing in MIMO-OFDM-based networks through the utilization of multi-sensor fusion techniques, tracking algorithms, and resource management. Specifically, we aim at exploiting range-angle radar maps derived from a collaborative set of BSs to track heterogeneous targets in a surveillance area. The main contributions of this work are as follows:

- With reference to a MIMO-OFDM system, we propose a data fusion technique to facilitate cooperative sensing

This work was presented in part at the European Radar Conference (EuRAD), Berlin, Germany, Sept. 2023.

This work was supported in part by the CNIT National Laboratory WiLab and the WiLab-Huawei Joint Innovation Center and in part by the European Union under the Italian National Recovery and Resilience Plan (NRRP) of NextGenerationEU, partnership on “Telecommunications of the Future” (PE00000001 - program “RESTART”).

E. Favarelli, E. Matricardi, L. Pucci, E. Paolini and A. Giorgetti are with the Dept. of Electrical, Electronic, and Information Eng. “Guglielmo Marconi” (DEI), University of Bologna, and WiLab, CNIT, Italy (e-mail: {elia.favarelli, elisabetta.matricardi3, lorenzo.pucci3, e.paolini, andrea.giorgetti}@unibo.it). W. Xu is with the Munich Research Center, Huawei Technologies Duesseldorf GmbH, Germany (e-mail: wen.dr.xu@huawei.com).

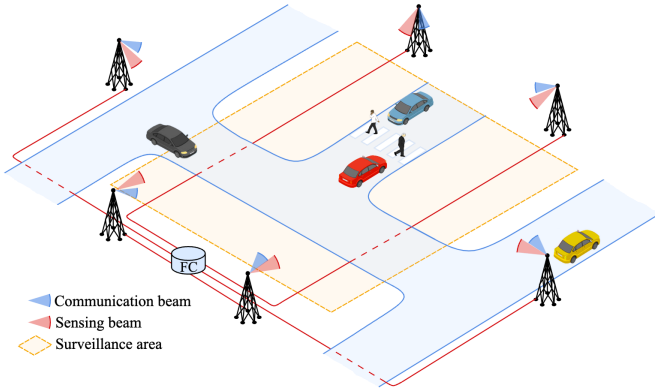


Figure 1. An urban scenario with six monostatic JSC BSs aiming at monitoring pedestrians (point-like targets) and vehicles (extended targets) in a surveillance area. BSs communicate with their UEs while simultaneously sensing the surrounding environment via dedicated sensing beams. The FC collects measurements from the BSs via the backhaul network, fuses them to create likelihood maps, and performs detection and multiple target tracking.

among monostatic JSC BSs by exchanging soft maps with a FC.

- We propose a thresholding strategy to control the amount of data shared between BSs and FC.
- We design a tailor-made three-step clustering procedure followed by a tracking algorithm to manage extended targets; we compare two tracking strategies, a probability hypothesis density (PHD) filter and a multi-Bernoulli mixture (MBM) filter.
- We explore the sensing/communication trade-off at the BS by varying the fraction of resources—power, frequency, and time—and provide insight into their impact on sensing and communication performance.
- To account for the complex channel propagation in an urban environment, we propose a channel model that considers multipath propagation in the BS-target-BS path and multiple reflection points to address extended targets such as vehicles.
- We assess the overall system capabilities using OSPA, downlink sum rate, and bit rate to evaluate localization performance, communication capabilities, and network communication overhead, respectively.

Capital and lowercase boldface letters denote matrices and vectors, respectively; \mathbf{I}_n is the $n \times n$ identity matrix; $\|\cdot\|_p$ stands for the p -norm; $\lfloor \cdot \rfloor$ represents the round operator; $\delta(\cdot)$ is the Dirac delta function; $(\cdot)^*$ stands for the conjugate, and $(\cdot)^T$ represents the transpose operation. A zero-mean circularly symmetric complex Gaussian random vector with covariance Σ is denoted by $\mathbf{x} \sim \mathcal{CN}(\mathbf{0}, \Sigma)$, and $\mathbf{x} \sim \mathcal{N}(\boldsymbol{\mu}, \Sigma)$ denotes the real-valued Gaussian random vector with mean $\boldsymbol{\mu}$ and covariance Σ .

The rest of the paper is organized as follows. Section II presents the JSC network for cooperative sensing system, focusing on the description of the system, channel, and target models. Section III describes the data fusion strategy, the clustering scheme, and the tracking algorithms. The performance of the proposed scheme is evaluated in Section IV, and conclusions are drawn in Section V.

II. SYSTEM MODEL

We consider a JSC network, illustrated in Fig. 1, which consists of multiple BSs operating at mmWave frequencies with monostatic sensing capability. Each BS transmits an OFDM waveform via multiple beams. In particular, while performing environment sensing through a dedicated beam and downlink signals, each BS simultaneously communicates with its UEs present in the scenario. Through the backhaul network, the BSs cooperate with a FC to accomplish targets' detection and tracking via data fusion. To mitigate inter-cell interference, frequency division and time-division are exploited among the BSs so that sensing beams do not interfere; this operation is usually performed also for communication.

To sense the surrounding environment, each BS uses a fraction of the available resources in the downlink. More precisely, the BS transmits multiple frames each consisting of M_s OFDM symbols with

$$\rho_f = K_s/K_0 \quad (1)$$

the fraction of subcarriers for JSC among the total K_0 available. The OFDM symbol duration T_s and the subcarrier spacing Δf are kept fixed. Multiple scans (measurements) of the surveillance area are performed to track the trajectory of the targets, with the time between two consecutive scans, T_{meas} , that can be varied to accommodate the communication/sensing trade-off. Hence, we indicate with

$$\rho_t = T_{\text{scan}}/T_{\text{meas}} \quad (2)$$

the fraction of time reserved for JSC.

Consequently, the transmitted signal in JSC slots can be represented by a matrix $\mathbf{X} \in \mathbb{C}^{K_s \times M_s}$, where the elements $x_{k,m}$ correspond to complex modulation symbols [14].

Without loss of generality, each BS is equipped with two uniform linear arrays (ULAs) with half wavelength spacing, one with N_T antennas for transmission and the other with N_R antennas for reception (see Fig. 3).

At the transmitter, the beamforming vector $\mathbf{w}_T \in \mathbb{C}^{N_T \times 1}$ is applied to data symbols at each antenna, resulting in $\mathbf{x}[k, m] = \mathbf{w}_T x_{k, m}$ [15]. Hence the communication beam (directed towards the UE) and the sensing beam (steered to scan the area) [14], [16] can be obtained by

$$\mathbf{w}_T = \sqrt{\rho_p} \mathbf{w}_{T,s} + \sqrt{1 - \rho_p} \mathbf{w}_{T,c} \quad (3)$$

where $\rho_p \in [0, 1]$ represents the fraction of power reserved for sensing in JSC slots, thus determining the fraction of power dedicated to communication, i.e., $1 - \rho_p$, while $\mathbf{w}_{T,s}$ and $\mathbf{w}_{T,c}$ are respectively the sensing and communication beamforming vectors. By considering a beam steering approach and performing a normalization with respect to the effective isotropic radiated power (EIRP) $P_T G_T^a$, the latter are

$$\mathbf{w}_{T,s} = \frac{\sqrt{P_T G_T^a}}{N_T} \mathbf{a}_T^*(\theta_{T,s}), \quad \mathbf{w}_{T,c} = \frac{\sqrt{P_T G_T^a}}{N_T} \mathbf{a}_T^*(\theta_{T,c})$$

where P_T is the transmit power, G_T^a is the transmit array gain along the beam steering direction, and $\mathbf{a}_T(\theta_{T,s}) \in \mathbb{C}^{N_T \times 1}$ and $\mathbf{a}_T(\theta_{T,c}) \in \mathbb{C}^{N_T \times 1}$ are the steering vectors for sensing and communication directions, $\theta_{T,s}$ and $\theta_{T,c}$, respectively [14].

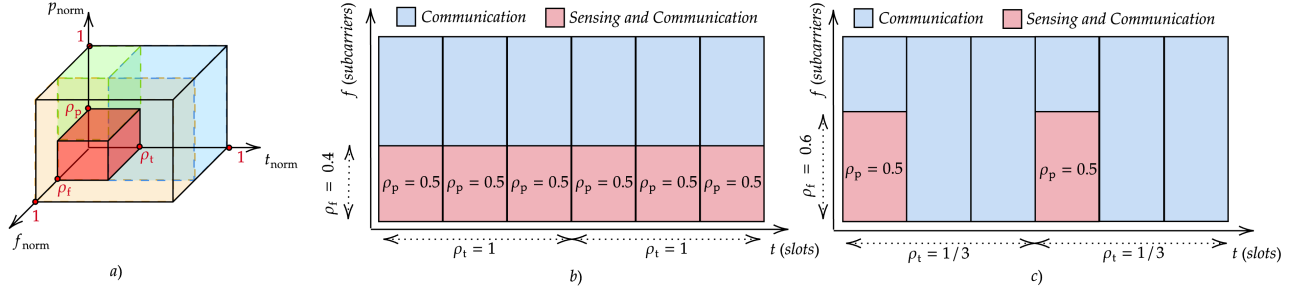


Figure 2. a) Graphical representation of the resource partition between communication and sensing at the BS. The red block represents the fraction of resources reserved for sensing, and the other blocks represent the remaining resources available for communication. b) Example of sensing and communication resource allocation in the time-frequency domain, with $\rho_p = 0.5$, $\rho_f = 0.4$, and $\rho_t = 1$. c) Another example with $\rho_p = 0.5$, $\rho_f = 0.6$, and $\rho_t = 1/3$.

Fig. 2 provides a graphical representation of the resource allocation for communication and JSC sensing and an example of the evolution of these resources over time. It is noteworthy that within the time-frequency slots designated for JSC, two scenarios can unfold: a) the slot is solely dedicated to sensing ($\rho_p = 1$); b) the slot accommodates one concurrent UE (i.e., one downlink communication beam), sharing resources with the sensing task according to (3).

At the sensing receiver, the symbols after OFDM demodulation are represented by

$$\mathbf{y}[k, m] = \mathbf{H}[k, m]\mathbf{x}[k, m] + \mathbf{n}[k, m] \quad (4)$$

where $\mathbf{H}[k, m] \in \mathbb{C}^{N_R \times N_T}$ is the channel matrix for the m th symbol and the k th subcarrier, and $\mathbf{n}[k, m] \sim \mathcal{CN}(\mathbf{0}, \sigma_n^2 \mathbf{I}_{N_R})$ is the noise vector at the receiving antennas. In the considered sensing direction, denoted as $\theta_{R,s} = \theta_{T,s}$, spatial combining is performed using the receiving beamforming vector $\mathbf{w}_R = \mathbf{a}_R^*(\theta_{R,s})$. This process results in the formation of a grid of received symbols denoted as $\mathbf{Y} \in \mathbb{C}^{K_s \times M_s}$, where each element $y_{k,m}$ is obtained by taking the inner product between the receiving beamforming vector \mathbf{w}_R and the vector of the symbols received at each antenna $\mathbf{y}[k, m]$, i.e., $y_{k,m} = \mathbf{w}_R^T \mathbf{y}[k, m]$. The collected symbols are subsequently used to generate range-angle maps as illustrated in Section II-C.

The spatial steering vectors $\mathbf{a}_T(\theta)$ and $\mathbf{a}_R(\theta)$ for a ULA with half-wavelength interelement spacing at a given angle of arrival (AoA)/angle of departure (AoD) θ is given by [17, Chapter 9], [15, Chapter 5]

$$\mathbf{a}_{T,R}(\theta) = \left[1, e^{j\pi \sin(\theta)}, \dots, e^{j\pi(N_a-1) \sin(\theta)} \right]^T$$

where N_a is the number of array antenna elements.

A. Multipath Channel Model

Let us begin by considering an anisotropic point-like scatterer labeled as l . This scatterer can either be a point-like target or a reflection point of a more complex object, referred to as an extended target. The channel model experienced during sensing is illustrated in Fig. 3. The signal emitted by the j th antenna propagates through the forward channel, from the BS to the scatterer, and is then reflected by the

scatterer, propagating back to the i th antenna at the BS via the backscatter channel.

In the presence of the sole direct path in both forward and backscatter channels, the linear time-variant MIMO channel¹ is represented in the frequency domain by the channel matrix $\mathbf{H}[k, m]$ in (4), which takes the form [14], [18], [19]

$$\mathbf{H}_l[k, m] = \nu_l(\psi_l) \alpha_l e^{j\phi_l} e^{j2\pi m T_s f_{D,l}} e^{-j2\pi k \Delta f \tau_l} \mathbf{a}_R(\theta_l) \mathbf{a}_T^T(\theta_l)$$

where τ_l , $f_{D,l}$, and θ_l are the round-trip delay, Doppler shift, and AoA/AoD of the i th (direct) Tx-scatterer-Rx path, respectively, while $\alpha_l \in \mathbb{R}$ is the gain which accounts for the path-loss (described by the radar equation as this is the sensing channel) and the radar cross-section (RCS) of the scatterer, and ϕ_l is a random phase. The function $\nu_l(\psi_l)$ capturing the scatterer anisotropy, is in the following dubbed visibility function, which accounts for angular-dependent reflection properties, where ψ_l is the AoA at the target side for the BS-scatterer link. Details will be provided in Section II-B. In the presence of multipath propagation represented by L_p paths between the BS and the scatterer, it can be shown that, due to linearity, the channel matrix in (4) becomes²

$$\mathbf{H}_l[k, m] = \sum_{p=0}^{L_p-1} \sum_{q=0}^{L_p-1} \nu_l(\psi_l^p) \nu_l(\psi_l^q) \xi_l^p \xi_l^q e^{j(\phi_l^p + \phi_l^q)} \times e^{j2\pi m T_s (f_{D,l}^p + f_{D,l}^q)} e^{-j2\pi k \Delta f (\tau_l^p + \tau_l^q)} \mathbf{a}_R(\theta_l^p) \mathbf{a}_T^T(\theta_l^q) \quad (5)$$

where ξ_l^r , ϕ_l^r , τ_l^r , $f_{D,l}^r$, and θ_l^r are the amplitude, phase, delay, Doppler shift, and AoA/AoD of the r th path (at the BS), respectively, while ψ_l^r are the angles at the scatterer side. The channel matrix (5) can be conveniently reformulated by separating the BS-scatterer-BS path (the one with $p = q = 0$), with $(\xi_l^0)^2 = \alpha_l$, from the diffuse component resulting into

¹The time-variant nature accounts for the Doppler effect due to target motion.

²An interesting interpretation provided in [20], [21] is that the overall channel impulse response (CIR) can be represented as the convolution between two CIRs: one from the so-called forward channel and the other from the backscatter channel. These CIRs are scaled by a factor that accounts for the path-loss and RCS of the target.

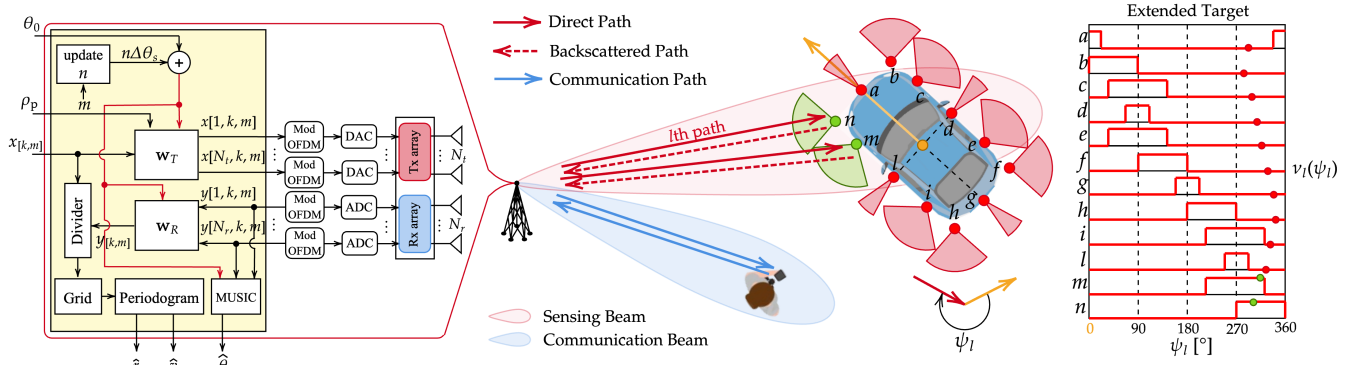


Figure 3. The MIMO-OFDM monostatic BS with multi-beam capability and a typical target vehicle. The vehicle is represented as an extended target made of distributed scatterers with specific visibility functions represented on the right.

$$\begin{aligned}
 \mathbf{H}_l[k, m] &= \underbrace{\nu_l(\psi_l) \alpha_l e^{j\phi_l} e^{j2\pi m T_s f_{D,l}} e^{-j2\pi k \Delta f \tau_l} \mathbf{a}_R(\theta_l) \mathbf{a}_T^T(\theta_l)}_{\text{direct path}} \\
 &+ \sum_{p=1}^{L_p-1} \sum_{q=1}^{L_p-1} \nu_l(\psi_l^p) \nu_l(\psi_l^q) \xi_l^p \xi_l^q e^{j(\phi_l^p + \phi_l^q)} \\
 &\times \underbrace{e^{j2\pi m T_s (f_{D,l}^p + f_{D,l}^q)} e^{-j2\pi k \Delta f (\tau_l^p + \tau_l^q)} \mathbf{a}_R(\theta_l^p) \mathbf{a}_T^T(\theta_l^q)}_{\text{diffuse component}}. \quad (6)
 \end{aligned}$$

Note that the diffuse component in (6) vanishes in the absence of multipath. Typically, the diffuse part remains unknown to the sensing receiver; thus, it can act as a disturbance, causing target smearing in the range-angle maps, as it will be shown in Section IV. Due to multiple paths, even a single scatterer is sensed as a superposition of various components with distinct delays, Doppler shifts, and AoAs, spreading the target across all three domains.

In the presence of L_s point-like targets or a single extended target modeled as a collection of L_s scatterers, the channel matrix becomes

$$\mathbf{H}[k, m] = \sum_{l=1}^{L_s} \mathbf{H}_l[k, m] \quad (7)$$

which contains L_s direct paths plus $L_s(L_p^2 - 1)$ diffuse paths.

B. Target Model

In this work, we consider a scenario featuring cars represented by the extended target model depicted in Fig. 3 and pedestrians as point-like targets. The channel matrix outlined in (6) and (7) accounts for the reflections caused by each scatterer, resulting in the generation of one or more backscattered signals. For each scatterer, the gain α_l includes the attenuation along the BS-scatterer-BS path, which can be related to the radar equation, and results in [17]

$$\alpha_l = \sqrt{\frac{c^2 \sigma_l}{(4\pi)^3 f_c^2 d_l^4}}$$

where d_l is the distance between the l th reflection point and the considered BS, and σ_l is its RCS, while f_c and c represent

the carrier frequency and the speed of light, respectively. The scatterers adhere to the Swerling I model, i.e., with probability density function (p.d.f.) given by [22]

$$f(\sigma_l) = \frac{1}{\bar{\sigma}_l} \exp\left(-\frac{\sigma_l}{\bar{\sigma}_l}\right) \quad \sigma_l \geq 0 \quad (8)$$

which is constant during the collection of a block of M_s symbols, and independent from block to block, with $\bar{\sigma}_l = \mathbb{E}\{\sigma_l\}$.

The pedestrian is modeled as a point-like target with $\bar{\sigma}_l = 0$ dBms. The car is an extended target consisting of $L_s = 12$ reflection points, including 4 reflections attributed to the front, back, and sides, each with a large RCS ($\bar{\sigma}_l = 20$ dBms). Additionally, there are 4 reflections associated with the wheelhouses ($\bar{\sigma}_l = 0$ dBms) and 4 reflections originating from the corners ($\bar{\sigma}_l = 5$ dBms) [23], [24]. Each scatterer is anisotropic, and its angle-dependent reflectivity is modeled through the visibility function $\nu_l(\psi_l)$, which characterizes the angular range where the scatterer exhibits an appreciable RCS; in contrast, the RCS is negligible outside that angular range. Recalling that ψ_l is the AoA at the target side for the BS-scatter link, for the car, $\nu_l(\psi_l) = 1$ for $\psi_l \in [\Psi_{\min,l}, \Psi_{\max,l}]$ and 0 elsewhere, with $\Psi_{\min,l}$ and $\Psi_{\max,l}$ defined for the specific scatterer type (e.g., corner, wheelhouse, etc.) [23], [24]. The visibility functions adopted in this work are shown in Fig. 3.

Note that the number of back-scattered signals varies over time because the number of reflections generated by the extended target depends on its position and orientation for the considered BS, according to the visibility function. Each scatterer, when visible, is associated with the RCS model in (8). Channels experienced by different scatterers are considered statistically independent; such an assumption is plausible because the scattering points of the extended target are spaced apart by several wavelengths at mmWave.

C. Range-Angle Map at the Base Station

To detect objects within the environment, each BS uses a combination of two beams specified by \mathbf{w}_T in (3). The communication beam is aimed at a particular UE, while the sensing beam is periodically steered within the range $[-\Theta, \Theta]$ with a fixed angular increment $\Delta\Theta$. A group of M_s OFDM symbols is transmitted to produce a range-angle map for every

sensing direction. The duration of a full scan, referred to as T_{scan} , is determined by the number of sensing orientations chosen and the duration of each OFDM symbol, T_s . After collecting all symbols in a given scan direction in the matrix \mathbf{Y} , the first stage is to perform reciprocal filtering, which consists of an element-wise division between the received and the transmitted grids, i.e., \mathbf{Y} and \mathbf{X} , to remove the dependence on the transmitted symbols and obtain a new matrix \mathbf{G} whose elements are [14], [25], [26]

$$g_{k,m} = \frac{y_{k,m}}{x_{k,m}} = \mathbf{w}_R^T \mathbf{H}[k,m] \mathbf{w}_T + \frac{\mathbf{w}_R^T \mathbf{n}[k,m]}{x_{k,m}}.$$

Then, a double-periodogram is computed on the rows and columns of \mathbf{G} to obtain a range-Doppler map, following the approach outlined in [14], [25], [27]. Given the relatively narrow beamwidth, we assume that only one scatterer will likely be present in each sensing direction. Therefore, the range-angle map is calculated by selecting the column of the periodogram with the maximum value, thereby associating it uniquely with the corresponding sensing direction.³

D. Network Capacity and Communication Overhead

The dual functional capability of the BS is ensured by considering frequency-division outlined in (1), time-division introduced in (2), and power-division reported in (3).

The assignment of resources to sensing inevitably influences communication performance. To assess this impact, we consider the aggregate capacity, defined as the downlink sum rate of each BS, calculated as⁴

$$\begin{aligned} C_{\text{DL}}(\rho_t, \rho_t, \rho_p) &= \rho_t \Delta f \sum_{k=1}^{\lfloor \rho_t K_0 \rfloor} C_{\text{JSC}} \left((1 - \rho_p) \text{SNR}_c^{(k)} \right) \\ &+ \rho_t \Delta f \sum_{k=\lfloor \rho_t K_0 + 1 \rfloor}^{K_0} \log_2(1 + \text{SNR}_c^{(k)}) \\ &+ (1 - \rho_t) \Delta f \sum_{k=1}^{K_0} \log_2(1 + \text{SNR}_c^{(k)}) \quad (9) \end{aligned}$$

where $\text{SNR}_c^{(k)}$ is the communication signal-to-noise ratio (SNR) experienced by the user at subcarrier k and $C_{\text{JSC}}(\gamma)$ is the capacity of the JSC slots. Indeed, while slots allocated for communication may use any constellation and the sum rate for them is calculated via the usual Shannon capacity, the JSC slots utilize a fixed constellation (in this case, quadrature phase shift keying (QPSK)) as it ensures high sensing performance because of its constant modulus [29].⁵

Sensing not only consumes resources at the radio segment, but cooperation among the BS, as illustrated in the next

³This is a low-complexity solution that can be readily replaced with alternative approaches such as 2D-MUSIC [28].

⁴To streamline the scenario we consider that each BS can use all the available resources.

⁵For QPSK signaling, a tight approximation of the capacity can be found in [30]:

$$C_{\text{JSC}}(\gamma) = 2(1 - a_1 e^{-b_1 \gamma} - a_2 e^{-b_2 \gamma})$$

where γ is the SNR, $a_1 = 0.143281$, $a_2 = 0.856719$, $b_1 = 1.557531$, and $b_2 = 0.57239$.

section, requires exchanging information via the backhaul contributing to network overhead. The overhead generated by the range-angle maps transmitted to the FC can be quantified as the average bit rate (averaged over the cooperating BSs)

$$R_b = \frac{N_b \rho_t}{T_{\text{meas}}} \frac{1}{N_s} \sum_{s=1}^{N_s} N_p^{(s)} \quad (10)$$

where N_s is the number of BSs, $N_p^{(s)}$ represents the number of map points shared by the s th BS and N_b is the number of bits used to encode each map point.

III. MULTI-SENSOR DATA FUSION AND TRACKING

A. Maps Fusion from Multiple Cooperating BSs

The strategy implemented to process the range-angle maps obtained by the network of JSC BSs is depicted in Fig. 4, and the map fusion sketched in Fig. 5. Each BS performs a uniform resampling procedure with grid resolution Δ_x and Δ_y to ensure consistent map fusion. Then, an excision filter with threshold γ_s is used to sift relevant map points (those related to regions where the score, or map intensity, is high) and reduce the network overhead due to map exchange with the FC. Hence, only selected pixels are shared with the FC. The effect of map excision and the related sensing/overhead trade-off will be addressed in Section IV.

At the FC, the resampled and filtered range-angle maps $\mathbf{L}_{s,t}$ are then combined using element-wise summation to obtain the soft map $\mathbf{L}_t = \frac{1}{N_s} \sum_{s=1}^{N_s} \mathbf{L}_{s,t}$, where t is the time index.

B. Clustering

The three-step clustering procedure used for performing detections from the soft maps and handling extended objects is illustrated in Fig. 4. In the first step, an excision filter is applied to the matrix \mathbf{L}_t with a threshold γ_d to retain map points with higher scores. In the second step, a k -nearest neighbors (k -NN) algorithm with $k = 1$ and a gate parameter ξ_{NN} is used to cluster points that are likely associated with previously detected targets (as discussed in [31]). The third step involves clustering of the remaining points, which are map points exceeding γ_d and lying outside the gate ξ_{NN} using the density-based spatial clustering of applications with noise (DBSCAN) algorithm. This algorithm specifies a maximum distance ξ_d for points to be considered part of the same cluster, as well as a minimum number of points, denoted as N_d , required to form a cluster (as described in [32]). It is important to note that DBSCAN is utilized in this context to cluster residual points that can represent potential new spawning targets. Lastly, each cluster centroid is stored in the matrix \mathbf{Z}_t , representing the target detections extracted from the soft maps.

C. Multi-target Tracking

In this section, we introduce the algorithms used for multi-target tracking, namely the PHD filter and the MBM filter. The following state vector represents each target state

$$\mathbf{s}_{t,n} = (s_{t,n,x}, s_{t,n,y}, s_{t,n,v_x}, s_{t,n,v_y})^T$$

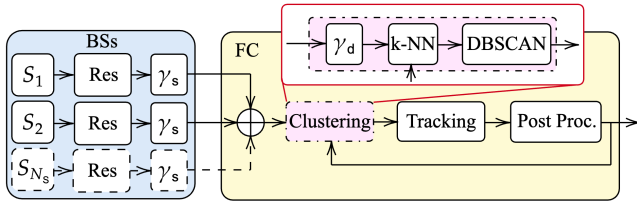


Figure 4. Block diagram of the processing chain. BSs and FC are depicted in blue and yellow, respectively.

where n is the target index. The first two elements of this vector correspond to the target position coordinates, while the last two represent the target velocity components. In this work, we update the target position components using information extracted from the map and calculate the target velocity by considering both the previous target position (at time $t-1$) and the current position.

1) *Probability Hypothesis Density Filter*: The PHD filter is a widely known algorithm for tracking [33]. A typical implementation approximates the target intensity function as a Gaussian mixture (GM) as [34]

$$D_{t-1|t-1}(\mathbf{x}) = \sum_{h=1}^{\mathcal{H}_{t-1|t-1}} w_{t-1|t-1}^{(h)} \mathcal{N}_{\mathbf{x}}(\boldsymbol{\mu}_{t-1|t-1}^{(h)}, \mathbf{P}_{t-1|t-1}^{(h)}) \quad (11)$$

where \mathbf{x} is a random finite set (RFS), $\mathcal{H}_{t-1|t-1}$ represents the number of Gaussian components in the prior intensity function, while $w_{t-1|t-1}^{(h)}$, $\boldsymbol{\mu}_{t-1|t-1}^{(h)}$, and $\mathbf{P}_{t-1|t-1}^{(h)}$, represent importance, mean and covariance of the h th component. The intensity function can be interpreted as a non-normalized p.d.f. whose integral returns the estimated number of targets in the scenario.

Linear Kalman prediction is used to infer the intensity function, i.e., $D_{t|t-1}(\mathbf{x})$, which can still be written in the form of equation (11), with parameters

$$\begin{aligned} w_{t|t-1}^{(h)} &= P_s w_{t-1|t-1}^{(h)} \\ \boldsymbol{\mu}_{t|t-1}^{(h)} &= \mathbf{F} \boldsymbol{\mu}_{t-1|t-1}^{(h)} \\ \mathbf{P}_{t|t-1}^{(h)} &= \mathbf{F} \mathbf{P}_{t-1|t-1}^{(h)} \mathbf{F}^T + \mathbf{Q} \end{aligned} \quad (12)$$

where P_s stands for the probability of survival of the target, \mathbf{F} represents the transition matrix that models the target behavior, and \mathbf{Q} is the covariance matrix that represents the motion uncertainty.

To build the predicted intensity function, the \mathcal{B} birth components must be added, representing the possibility of new targets spawning in the surveillance area. The total number of components after prediction is then $\mathcal{H}_{t|t-1} = \mathcal{H}_{t-1|t-1} + \mathcal{B}$.

The predicted components are then updated with the measurements \mathbf{Z}_t extracted from the map \mathbf{L}_t , as described in Section III-B. Firstly, the Kalman filter parameters are derived as

$$\begin{aligned} \hat{\mathbf{z}}_{t|t-1}^{(h)} &= \mathbf{H} \boldsymbol{\mu}_{t|t-1}^{(h)} \\ \mathbf{S}_{t,m}^{(h)} &= \mathbf{R}_{t,m} + \mathbf{H} \mathbf{P}_{t|t-1}^{(h)} \mathbf{H}^T \\ \mathbf{K}_{t,m}^{(h)} &= \mathbf{P}_{t|t-1}^{(h)} \mathbf{H}^T (\mathbf{S}_{t,m}^{(h)})^{-1} \end{aligned} \quad (13)$$

where \mathbf{H} represents the measurement matrix, $\hat{\mathbf{z}}_{t|t-1}^{(h)}$ is the h th predicted measurement, $\mathbf{S}_{t,m}^{(h)}$ is the innovation covariance, $\mathbf{R}_{t,m}$ represents the m th measurement covariance, and $\mathbf{K}_{t,m}^{(h)}$ is the Kalman gain. Then, each component in the predicted intensity function is updated with each measurement $\mathbf{z}_{t,m}$ in the measurements matrix \mathbf{Z}_t , by

$$\begin{aligned} \tilde{w}_{t|t}^{(j)} &= P_d w_{t|t-1}^{(h)} \mathcal{N}_{\mathbf{z}_{t,m}}(\hat{\mathbf{z}}_{t|t-1}^{(h)}, \mathbf{S}_{t,m}^{(h)}) \\ \boldsymbol{\mu}_{t|t}^{(j)} &= \boldsymbol{\mu}_{t|t-1}^{(h)} + \mathbf{K}_{t,m}^{(h)} (\mathbf{z}_{t,m} - \hat{\mathbf{z}}_{t|t-1}^{(h)}) \\ \mathbf{P}_{t|t}^{(j)} &= (\mathbf{I} - \mathbf{K}_{t,m}^{(h)} \mathbf{H}) \mathbf{P}_{t|t-1}^{(h)} \end{aligned}$$

where P_d represents the probability of detection, and $\mathcal{N}_{\mathbf{z}_{t,m}}(\hat{\mathbf{z}}_{t|t-1}^{(h)}, \mathbf{S}_{t,m}^{(h)})$ stands for the m th measurement likelihood with respect to the h th component. Weights are then normalized as

$$w_{t|t}^{(j)} = \frac{\tilde{w}_{t|t}^{(j)}}{\lambda_c + \sum_{k=1}^{\mathcal{H}_{t|t-1}} \tilde{w}_{t|t}^{(k)}}$$

where λ_c represents the clutter intensity, which is modelled as a Poisson point process (PPP) [35]. To account for missed detections, an additional set of components is added to the posterior, i.e.,

$$w_{t|t}^{(h)} = (1 - P_d) w_{t|t-1}^{(h)}, \quad \boldsymbol{\mu}_{t|t}^{(h)} = \boldsymbol{\mu}_{t|t-1}^{(h)}, \quad \mathbf{P}_{t|t}^{(h)} = \mathbf{P}_{t|t-1}^{(h)}.$$

The number of components in the posterior can be written as $\mathcal{H}_{t|t} = \mathcal{H}_{t|t-1} (M_t + 1)$, where M_t stands for the number of measurements at time instant t . Hence, the number of targets is estimated via

$$\hat{N}_{\text{obj}} = \left\lceil \sum_{h=1}^{\mathcal{H}_{t|t}} w_{t|t}^{(h)} \right\rceil$$

while the n th target state estimation is obtained by

$$\hat{\mathbf{s}}_{t,n} = \underset{w_{t|t}^{(h)}}{\operatorname{argmax}} \boldsymbol{\mu}_{t|t}^{(h)}.$$

2) *Multi-Bernoulli Mixture Filter*: The MBM filter is an alternative to the PHD filter in multiple target tracking problems that exploits the association probability between measurements and targets [36]. Let us consider the following MBM distribution to represent the prior multiobject p.d.f.

$$\text{MBM}_{t-1|t-1}(\mathbf{x}) = \sum_{g=1}^{\mathcal{G}_{t-1|t-1}} w_{t-1|t-1}^{(g)} \text{MB}_{t-1|t-1}^{(g)}(\mathbf{x}) \quad (14)$$

where $\mathcal{G}_{t-1|t-1}$ represents the number of multi-Bernoulli (MB) components or global hypotheses and $w_{t-1|t-1}^{(g)}$ stands for the g th component importance. The MB distribution (14) can be written as

$$\text{MB}_{t-1|t-1}^{(g)}(\mathbf{x}) = \sum_{\uplus \mathbf{x}_l = \mathbf{x}} \prod_{l=1}^{\mathcal{L}_{t-1|t-1}^{(g)}} \text{B}_{t-1|t-1}^{(g,l)}(\mathbf{x}_l) \quad (15)$$

where $\mathcal{L}_{t-1|t-1}^{(g)}$ is the number of Bernoulli components or local hypotheses, and the summation is performed over all possible unions of mutually disjoint RFSs that generate \mathbf{x} ,

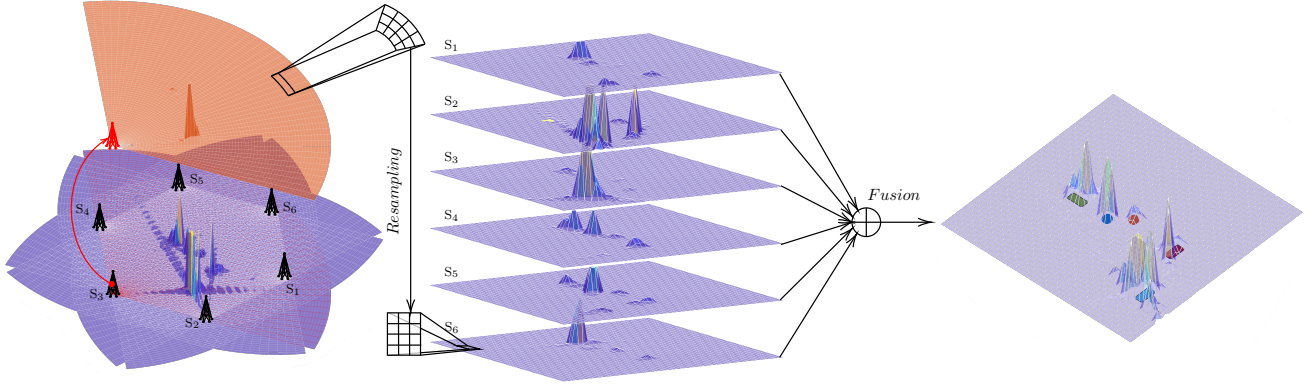


Figure 5. Soft map fusion strategy. The maps shown are obtained from the simulations reported in the numerical results considering the vehicle scenario described in Section IV.

i.e., all possible data associations between measurements and targets [36]. Each component in (15) can be written as

$$\mathbf{B}_{t-1|t-1}^{(g,l)}(\mathbf{x}_l) = r_{t-1|t-1}^{(g,l)} \mathcal{N}_{\mathbf{x}_l}(\boldsymbol{\mu}_{t-1|t-1}^{(g,l)}, \mathbf{P}_{t-1|t-1}^{(g,l)})$$

where $r_{t-1|t-1}^{(g,l)}$ is the existence probability of the l th local hypothesis in the g th global hypothesis, while $\boldsymbol{\mu}_{t-1|t-1}^{(h)}$ and $\mathbf{P}_{t-1|t-1}^{(h)}$ represent the mean and the covariance of the considered component, respectively. Overall, the MBM distribution can be represented with the following set of parameters:

$$\{w_{t-1|t-1}^{(g)}, \{r_{t-1|t-1}^{(g,l)}, \boldsymbol{\mu}_{t-1|t-1}^{(g,l)}, \mathbf{P}_{t-1|t-1}^{(g,l)}\}_{l=1}^{\mathcal{L}_{t-1|t-1}^{(g)}}\}_{g=1}^{\mathcal{G}_{t-1|t-1}}.$$

Similarly to (12) a Kalman prediction is performed to infer the parameters at time t as follows

$$\begin{aligned} w_{t|t-1}^{(g)} &= w_{t-1|t-1}^{(g)}, \quad r_{t|t-1}^{(g,l)} = P_s r_{t-1|t-1}^{(g,l)} \\ \boldsymbol{\mu}_{t|t-1}^{(g,l)} &= \mathbf{F} \boldsymbol{\mu}_{t-1|t-1}^{(g,l)}, \quad \mathbf{P}_{t|t-1}^{(g,l)} = \mathbf{F} \mathbf{P}_{t-1|t-1}^{(g,l)} \mathbf{F}^T + \mathbf{Q}. \end{aligned} \quad (16)$$

To account for new spawning targets, a set of \mathcal{B} Bernoulli components is added to each global hypothesis. The overall number of components after the prediction step is $(\mathcal{L}_{t-1|t-1} + \mathcal{B})\mathcal{G}_{t-1|t-1}$. In the update phase, firstly, Kalman filter parameters are derived, i.e.,

$$\begin{aligned} \hat{\mathbf{z}}_{t|t-1}^{(g,l)} &= \mathbf{H} \boldsymbol{\mu}_{t|t-1}^{(g,l)} \\ \mathbf{S}_{t,m}^{(g,l)} &= \mathbf{R}_{t,m} + \mathbf{H} \mathbf{P}_{t|t-1}^{(g,l)} \mathbf{H}^T \\ \mathbf{K}_{t,m}^{(g,l)} &= \mathbf{P}_{t|t-1}^{(g,l)} \mathbf{H}^T (\mathbf{S}_{t,m}^{(g,l)})^{-1}. \end{aligned} \quad (17)$$

Then, each component in the predicted MBM distribution is updated with measurements. Let us define the association vector $\boldsymbol{\theta}_i$ for the g th global hypothesis, whose elements $\theta_{i,j} = m$ represent the association between the l th measurement and the m th Bernoulli component. If a hypothesis is associated with a missed detection, its association vector elements $\theta_{i,j}$ is set to 0. Each association hypothesis represents a new component in the MBM posterior. During update, if a component is associated

with a measurement, i.e., $\theta_{i,j} \neq 0$, that component parameters are updated according to

$$\begin{aligned} r_{t|t}^{(i,j)} &= 1 \\ \boldsymbol{\mu}_{t|t}^{(i,j)} &= \boldsymbol{\mu}_{t|t-1}^{(h)} + \mathbf{K}_{t,m}^{(g,l)} (\mathbf{z}_{t,m} - \hat{\mathbf{z}}_{t|t-1}^{(g,l)}) \\ \mathbf{P}_{t|t}^{(i,j)} &= (\mathbf{I} - \mathbf{K}_{t,m}^{(g,l)} \mathbf{H}) \mathbf{P}_{t|t-1}^{(g,l)}. \end{aligned}$$

Conversely, if a component is associated to a missed detection, i.e., $\theta_{i,j} = 0$, then the parameters of this component are updated as follows

$$\begin{aligned} r_{t|t}^{(i,j)} &= \frac{r_{t|t-1}^{(g,l)} (1 - P_d)}{1 - r_{t|t-1}^{(g,l)} + r_{t|t-1}^{(g,l)} (1 - P_d)} \\ \boldsymbol{\mu}_{t|t}^{(i,j)} &= \boldsymbol{\mu}_{t|t-1}^{(g,l)} \\ \mathbf{P}_{t|t}^{(i,j)} &= \mathbf{P}_{t|t-1}^{(g,l)}. \end{aligned}$$

It is a common practice to define log-weights $l_{t|t-1}^{(g)} = \log(w_{t|t-1}^{(g)})$ to avoid numerical problems in the posterior weight computation [37]. For a given measurement association $\theta_{i,j} = m$ in the association vector, we can compute its posterior log-weight as

$$l_{t|t-1}^{(i,j)} = \log(r_{t|t-1}^{(g,l)} P_d \lambda_c^{-1} \mathcal{N}_{\mathbf{z}_{t,m}}(\mathbf{H} \boldsymbol{\mu}_{t|t-1}^{(g,l)}, \mathbf{S}_{t,m}^{(g,l)}))$$

and in case of missed detection, $\theta_{i,j} = 0$, as

$$l_{t|t-1}^{(i,j)} = \log(1 - r_{t|t-1}^{(g,l)} + r_{t|t-1}^{(g,l)} (1 - P_d)).$$

The overall non-normalized posterior log-weight for an entire association hypothesis $\boldsymbol{\theta}_i$ is given by

$$\tilde{l}_{t|t}^{(i)} = l_{t|t-1}^{(g)} + \sum_{j:\theta_{i,j} \neq 0} \tilde{l}_{t|t-1}^{(i,j)} + M_t \log(\lambda_c)$$

where

$$\tilde{l}_{t|t-1}^{(i,j)} = \begin{cases} l_{t|t-1}^{(i,j)} - \log(\lambda_c) & \text{if } \theta_{i,j} = 0 \\ l_{t|t-1}^{(i,j)} & \text{otherwise.} \end{cases}$$

Then, the normalized log-weights can be computed as follows

$$l_{t|t}^{(i)} = \tilde{l}_{t|t}^{(i)} - \tilde{l}_{t|t}^{(i^*)} - \log \sum_i \exp(\tilde{l}_{t|t}^{(i)} - \tilde{l}_{t|t}^{(i^*)})$$

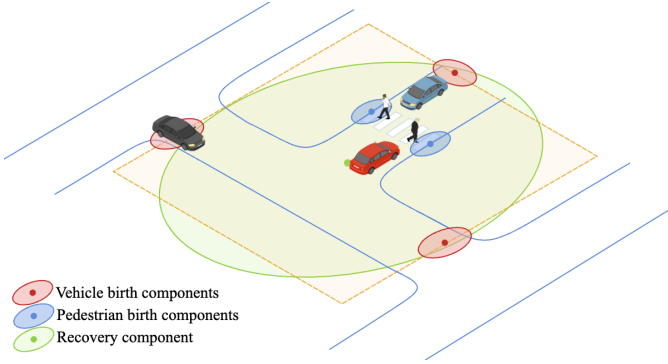


Figure 6. Birth components for tracking algorithms. Red ellipsoids stand for vehicle birth components, and blue ones represent pedestrian birth components. The green component that covers all the surveillance area is necessary to restore tracks that disappeared due to consecutive missed detections.

where i^* is the index related to the maximum log-weight. Estimations $\hat{s}_{t,n}$ are finally extracted from the posterior distribution, considering the mean value $\mu_{t|t}^{(i,j)}$ of the MB components with probability of existence $r_{t|t}^{(i,j)} \geq \gamma_e$ from the MBM component with highest probability $w_{t|t}^{(i)}$.

3) *Birth and Death Model*: To capture new targets appearing in the surveillance area, a set of Gaussian components are generated for the PHD filter intensity function, as well as Bernoulli components are generated for the MBM p.d.f., respectively, as

$$\{w^{(b)}, \mu^{(b)}, \mathbf{P}^{(b)}\}_{b=1}^{\mathcal{C}_b}, \{r^{(b)}, \mu^{(b)}, \mathbf{P}^{(b)}\}_{b=1}^{\mathcal{B}}.$$

Such components can be generated considering prior information about the environment. For example, in a vehicular scenario, the number of hypotheses and their mean value, covariance, and importance are set based on the lanes and crosswalks in the environment as sketched in Fig. 6.

Target death is modeled through a constant probability of survival P_s . During prediction, if a component is associated with a missed detection, its weight is multiplied by a factor proportional to P_s , which means that consecutive missed detections lead to unlikely target state components.

4) *Motion Model*: A linear prediction model is selected to track the behavior of both extended and point-like targets. This is justified by the value of T_{scan} relative to the target velocity, which allows approximating the motion of the target as linear among consecutive acquisitions (see Section IV). The transition matrix and process noise covariance matrix adopted in (12) and (16) are $\mathbf{F} = [1, 0, T_{\text{scan}}, 0; 0, 1, 0, T_{\text{scan}}; 0, 0, 1, 0; 0, 0, 0, 1]$ and $\mathbf{Q} = \alpha_q T_{\text{scan}} \mathbf{I}_4$, where α_q is a parameter that represents the prediction uncertainty about the target motion.

5) *Measurement Model*: As stated, only the position information about the targets is extracted from measurements, while velocity is inferred from consecutive position measurements. Therefore, considering a linear measurement model, the measurement matrix $\mathbf{H} = [1, 0, 0, 0; 0, 1, 0, 0]$ is considered in (13) and (17). Due to high-resolution maps that generate more detections from each target, the measurement covariance matrix is evaluated from the detection distribution

to take advantage of the information contained in multiple detections. Let us define the set of map points \mathbf{L}_t associated to a particular measurement extracted after clustering $\mathbf{z}_{t,m}$ as $\mathbf{L}_t^{(\mathbf{z}_{t,m})}$. The covariance measurement matrix in (13) and (17) is then evaluated as $\mathbf{R}_t = (N_{\mathbf{z}_{t,m}} - 1)^{-1} \sum_{n=1}^{N_{\mathbf{z}_{t,m}}} (\mathbf{l}_{t,n}^{(\mathbf{z}_{t,m})} - \mathbf{z}_{t,m})(\mathbf{l}_{t,n}^{(\mathbf{z}_{t,m})} - \mathbf{z}_{t,m})^\top$, where $N_{\mathbf{z}_{t,m}}$ represents the number of maps points associated to the measurements $\mathbf{z}_{t,m}$, and $\mathbf{l}_{t,n}^{(\mathbf{z}_{t,m})}$ is the n th map point in the set $\mathbf{L}_t^{(\mathbf{z}_{t,m})}$.

D. Post Processing

In order to control the complexity of the algorithms and to achieve a good estimation accuracy, a set of post processing procedures must be implemented.

In the PHD filter, pruning, capping, and merging are sequentially implemented to reduce the number of components in the posterior intensity function. Firstly, pruning is implemented by removing all components in the posterior whose weights $w_{t|t}^{(h)}$ are below a predefined threshold γ_p . Then, capping is performed on the remaining components, selecting at most the γ_q components with greatest $w_{t|t}^{(h)}$ values, fixing the maximum number of components in the posterior to γ_q . Finally, on the remaining components survived after capping, merging is implemented as follows

$$w_{t|t}^{(k)} = \sum_{i \in \zeta_m} w_{t|t}^{(i)}, \quad \mu_{t|t}^{(k)} = \sum_{i \in \zeta_m} w_{t|t}^{(i)} \mu_{t|t}^{(i)}$$

$$\mathbf{P}_{t|t}^{(k)} = \sum_{i \in \zeta_m} w_{t|t}^{(i)} \mathbf{P}_{t|t}^{(i)} + (\mu_{t|t}^{(i)} - \mu_{t|t}^{(k)})(\mu_{t|t}^{(i)} - \mu_{t|t}^{(k)})^\top$$

where k is the new index assigned to the derived component and i is the index of the merged component. ζ_m is a set containing the components that must be merged, i.e., whose mean value distance satisfies $\|\mu_{t|t}^{(i)} - \mu_{t|t}^{(j)}\|_2 < \gamma_v$.

In the MBM filter, during the update phase, a gate for eligible data associations is implemented, pruning all the association hypotheses with $w_{t|t}^{(k)} < \xi_a$. Both the MBM and the MB are pruned with threshold γ_g and γ_l , respectively. The residual MBM components are capped with threshold γ_c . For the sake of increasing estimation accuracy, in the most likely MBM component, the MB components closer than γ_m are merged as previously described.

IV. NUMERICAL RESULTS

In this section, we present numerical results to explore the interplay between communication and sensing. We investigate the impact of the amount of power dedicated to sensing ρ_p , the fraction of subcarriers ρ_f and the fraction of time ρ_t . Moreover, the cost/benefits of cooperation is investigated by varying the sharing threshold γ_s .

A. Performance Metrics

The dual-function system is investigated under three perspectives: communication performance, communication overhead, and sensing performance. The communication performance is evaluated through the sum rate in (9), which measures the downlink network capacity of each BS given a

Table I
SYSTEM PARAMETERS

Base station		
Δ_x, Δ_y	Resampling grid resolution	0.1 m
N_s	Number of base stations	6
T_{scan}	Scan period	0.05 s
ρ_p	Fraction of power reserved for sensing	
ρ_t	Fraction of time reserved for sensing	
ρ_f	Fraction of frequency reserved for sensing	
γ_s	Sharing threshold	V^2/Hz
N_b	Number of bits	16
Clustering		
γ_d	Detection threshold	$2 \cdot 10^{-7} V^2/\text{Hz}$
ξ_{NN}	Gate k-NN	5 m
ξ_d	Gate DBSCAN	3 m
N_d	Minimum number of points DBSCAN	50
Tracking		
λ	Clutter intensity	0.001
\mathbf{H}	Measurement matrix	
\mathbf{F}	Transition matrix	
\mathbf{R}_t	Measurements covariance	
\mathbf{Q}	Process noise covariance	
α_q	Prediction uncertainty	5
P_d	Probability of detection	0.99
P_s	Probability of survival	0.9
γ_e	Existing threshold	0.99
γ_p	Pruning PHD components	$100 \cdot 10^{-6}$
γ_q	Capping PHD components	10
γ_v	Merging PHD components	5
ξ_a	Gate admissible associations	14
γ_g	Pruning MBM components	10^{-15}
γ_l	Pruning MB components	$100 \cdot 10^{-6}$
γ_c	Capping MBM components	10
γ_m	Merging MB components	5
OSPA metric		
p	OSPA order	2
ξ_g	OSPA gate	5

particular set of resources reserved for communication. The cost of sensing is estimated in terms of sum rate reduction and network overhead, as per (10), due to sharing sensing data among the BSs. Since a complex scenario with multiple point-like and extended targets and multipath propagation is considered, the OSPA metric is used to evaluate the sensing performance of the network, also in terms of cooperation gain. This metric is widely used to evaluate the performance of tracking algorithms in multi-target (or multi-scatterer) scenarios, as it allows to combine localization and detection performance into a single metric, taking into account false alarms and missed detections [38]. The p -order OSPA metric is defined as [39], [40]

$$\text{OSPA} = \left[\frac{1}{N_c} \left(\sum_{(i,j) \in \zeta_g^*} \|\mathbf{s}_{t,i} - \hat{\mathbf{s}}_{t,j}\|_p^p + \frac{\xi_g^p}{2} (|\mathbf{S}_t| + |\hat{\mathbf{S}}_t| - 2|\zeta_g^*|) \right) \right]^{\frac{1}{p}} \quad (18)$$

where $\hat{\mathbf{S}}_t$ represents the first two rows of $\hat{\mathbf{S}}_t$ which is a matrix containing the estimated state vectors of all the detected targets

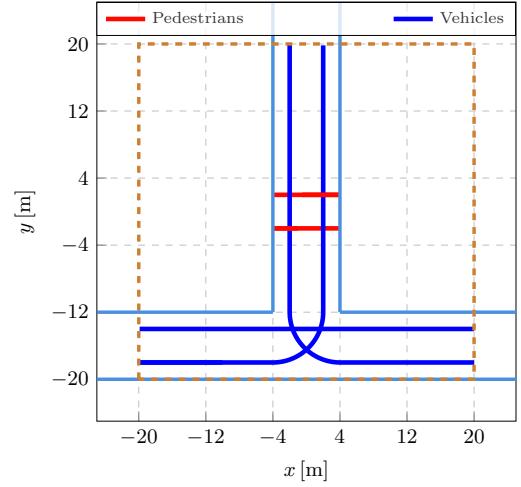


Figure 7. Targets behavior in the considered scenario. Orange dashed square represents the surveillance area while light blue lines represent lanes.

at time t ; hence $\hat{\mathbf{S}}_t$ retains only the estimated target positions. Moreover, the parameter ξ_g represents the OSPA gate: estimated positions that are further than ξ_g from the actual target positions are considered as false alarms and, dually, real target positions that are not associated with any estimates (because not inside the gate) will be counted as missed detections. The vector ζ_g^* represents the best assignment between the estimated set of objects $\hat{\mathbf{S}}_t$ and the true ones \mathbf{S}_t , while $|\mathbf{S}_t|$, $|\hat{\mathbf{S}}_t|$, and $|\zeta_g^*|$ are the cardinality of the considered set, namely, the number of objects in the estimated state vector, the ground truth cardinality, and the data association vector, respectively. Finally, N_c is the number of elements in the OSPA metric given by $N_c = |\mathbf{S}_t| + |\hat{\mathbf{S}}_t| - |\zeta_g^*|$.

When $p = 2$, the first term in (18) can be interpreted as the mean square error between the estimated and actual target positions. Instead, the second term can be rewritten as

$$\frac{\xi_g^p}{2} (|\mathbf{S}_t| - |\zeta_g^*|) + \frac{\xi_g^p}{2} (|\hat{\mathbf{S}}_t| - |\zeta_g^*|)$$

such that the first term is proportional to the probability of missed detections, while the second one is related to the probability of false alarms, which are defined as

$$P_D = \frac{|\zeta_g^*|}{|\mathbf{S}_t|}, \quad P_{\text{FA}} = \frac{|\hat{\mathbf{S}}_t| - |\zeta_g^*|}{|\mathbf{S}_t|}, \quad P_{\text{MD}} = 1 - P_D.$$

B. System and Scenario Parameters

We considered a vehicular scenario with 6 BSs and a set of extended and point-like targets, whose behavior is depicted in Fig. 7. Pedestrians move with uniform linear motion, whereas vehicles' motion is modeled alternating static, accelerated/decelerated linear, uniform linear, and uniform circular motions. The area monitored is a typical urban crossroad of 1600 m^2 , with $x \in [-20, 20] \text{ m}$ and $y \in [-20, 20] \text{ m}$. The main parameters are summarized in Table I.

The transmission parameters are: QPSK modulation, $f_c = 28 \text{ GHz}$, $\Delta f = 120 \text{ kHz}$, $K_0 = 3168$ (i.e., about 400 MHz

bandwidth), $M = 1120$, and $M_s = 112$. The EIRP is set to 30 dBm, and the one-sided noise power spectral density (PSD) is $N_0 = 4 \cdot 10^{-20}$ W/Hz. The BSs are equipped with $N_T = N_R = 50$ antennas. Note that in (9), without loss of generality, we assume that all UEs experience the same SNR, and the channel is considered flat, therefore, $\text{SNR}_c^{(k)} = 8$ dB for all k .

The multipath propagation is simulated using the 3GPP 38.901 urban micro-cell line-of-sight (LOS) scenario [41]. Parameters such as ξ_l^r , ϕ_l^r , τ_l^r , $f_{D,l}^r$, θ_l^r , and ψ_l^r are generated using QUasi Deterministic RadIo channel GenerAtor (QuaDRiGa) software [42] for each target and position along the trajectories. Specifically, for each scatterer, the model considers the direct path and the 5 strongest paths of the diffuse component, for a total of $L_T = 6$ paths. This results in a monostatic CIR with $L_T^2 = 36$ paths, as per (5).

The six BSs are positioned along a circumference with a radius of 50 m, centered on the surveilled area. Their ULAs are tangent to the circumference (i.e., orthogonal to the radius), providing a scanning area of 120° with a maximum sensing distance of 85 m to prevent inter-symbol interference (ISI). Each BS performs a scan lasting $T_{\text{scan}} = 50$ ms, and the overall scene is monitored for 10 s, resulting in the collection of $N_m = 200$ measurements (maps). The grid resolution is set to $\Delta_x = 0.1$ m and $\Delta_y = 0.1$ m. The number of bits selected to represent each map point is set to $N_b = 16$. The sensing beam is periodically steered within the range $[-\Theta, \Theta]$, where $\Theta = 60^\circ$, with a fixed angular increment of $\Delta\Theta = 2.4^\circ$.

In the clustering algorithm, the detection threshold is set to $\gamma_d = 2 \cdot 10^{-7}$ V²/Hz, in k-NN the gate is set to $\xi_{\text{NN}} = 5$, and in DBSCAN the cutoff distance and the minimum number of points to form the cluster are $\psi_d = 3$ and $N_d = 50$, respectively.

In both tracking algorithms, the clutter intensity is set to $\lambda_c = 0.1$, the prediction uncertainty to $\alpha_q = 5$, the initial components covariance to $\mathbf{P} = 0.5 \cdot \mathbf{I}_4$, and the probabilities of detection and survival are $P_d = 0.99$ and $P_s = 0.9$, respectively.

In the PHD filter, the components pruning threshold is $\gamma_p = 100 \cdot 10^{-6}$ while the maximum number of components is fixed to $\gamma_q = 10$. The birth components for new appearing objects are initialized with importance $w^{(b)} = 0.1$ and covariance $\mathbf{P}^{(b)} = 0.1 \cdot \mathbf{I}_4$, with position $\boldsymbol{\mu}^{(b)}$ reflecting the components depicted in Fig 6. The recovery component is initialized with importance $w^{(b)} = 0.01$ and covariance $\mathbf{P}^{(b)} = 5 \cdot \mathbf{I}_4$. The merging threshold is set to $\gamma_v = 5$.

In the MBM filter, the pruning threshold on the probability of existence is $\gamma_1 = 100 \cdot 10^{-6}$ while the pruning threshold on the MBM components is set to $\gamma_g = 10^{-15}$. The maximum number of MBM components is fixed to $\gamma_c = 10$. The gate for the admissible associations is set to $\xi_a = 14$. The existence threshold is set to $\gamma_e = 0.99$. The birth components for new appearing objects are initialized with a probability of existence $r^{(b)} = 10^{-4}$ and covariance $\mathbf{P}^{(b)} = 0.1 \cdot \mathbf{I}_4$, with position $\boldsymbol{\mu}^{(b)}$ reflecting again the components reported in Fig 6. The recovery component is initialized with importance $r^{(b)} = 10^{-5}$ and covariance $\mathbf{P}^{(b)} = 5 \cdot \mathbf{I}_4$. The merging threshold is set to $\gamma_m = 5$.

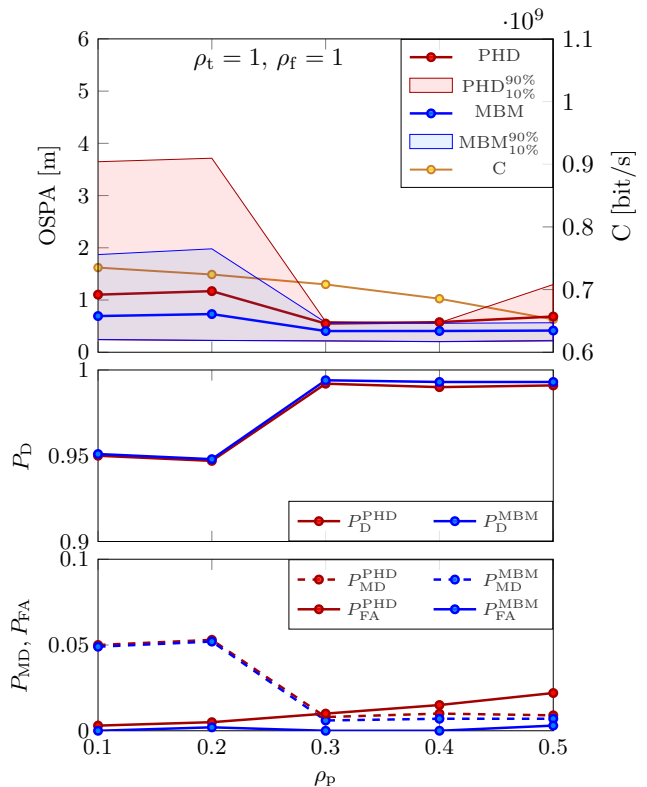


Figure 8. Communication and sensing performance varying the fraction of power reserved for JSC ρ_p . The downlink capacity is per BS.

C. Impact of the Fraction of Power ρ_p

In Fig. 8, the tracking and communication performance are reported by varying the fraction of power dedicated to sensing, ρ_p , when $\rho_f = 1$ and $\rho_t = 1$.

At the top, the average OSPA metric is displayed for both tracking algorithms in red and blue, respectively. The yellow curve represents the downlink sum rate defined in (9). The blue and red areas represent the range of values between the 90th and 10th percentiles of the OSPA distance. The detection probability of the tracking algorithms is shown in the middle plot, while the missed detection probability and false alarm probability are presented at the bottom. This structure is repeated for all subsequent figures.

Both PHD and MBM filters perform similarly for varying ρ_p . Specifically, at low values of ρ_p , weak targets such as pedestrians disappear, leading to increased missed detection. It is interesting to note that for large values of ρ_p (e.g., 0.5), the localization error experiences a slight increase. This is due to increased false alarms caused by multipath propagation, which becomes more relevant by increasing the sensing transmission power.

From a communication perspective, increasing ρ_p results in lower downlink capacity, as expected. For a value of $\rho_p = 0.1$, the localization error is around 1 m, while the downlink capacity is 0.72 Gbit/s. Increasing ρ_p to 0.4 halves the OSPA error while reducing the network capacity to 0.68 Gbps, which represents a 6% loss in communication performance.

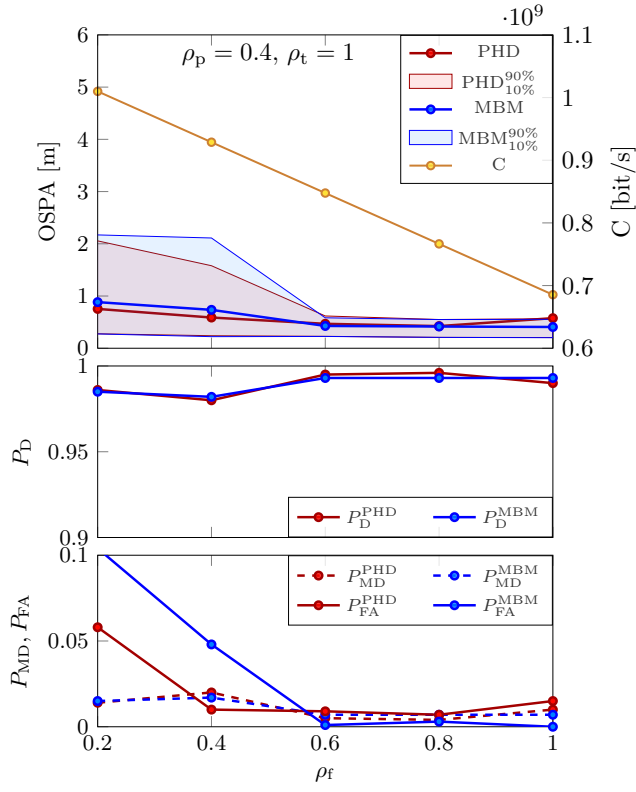


Figure 9. Communication and sensing performance varying the fraction of subcarriers reserved for JSC ρ_f . The downlink capacity is per BS.

D. Impact of the Fraction of Subcarriers ρ_f

Communication and sensing performance, varying the frequency resources allocation between the two functions, are depicted in Fig. 9, considering $\rho_p = 0.4$ and $\rho_t = 1$.

From a sensing perspective, it is interesting to observe that as ρ_f decreases, the OSPA increases due to a higher probability of false alarm. This effect can be attributed to a lower map resolution due to a lower bandwidth, resulting in target smearing that can more likely generate false target spawns.

For communication, a decrease of ρ_f results in an increase of the fraction of subcarriers exclusively dedicated to communication, which leads to a higher downlink sum rate. A capacity of 1 Gbit/s is ensured by fixing $\rho_f = 0.2$, with a localization error around 0.9 m. Increasing ρ_f to 0.6, the localization error drops to 0.5 m, with a reduction in network capacity of 15%, i.e., 0.15 Gbit/s.

E. Impact of the Fraction of Time ρ_t

In Fig. 10, communication and sensing performance are presented, varying the fraction of time devoted to JSC, ρ_t , with $\rho_p = 0.4$ and $\rho_f = 0.6$.

Notably, as ρ_t decreases, an increase in the OSPA error for both tracking algorithms can be observed. This increase can be attributed to a higher probability of missed detections, due to less accurate motion prediction. In this setup, the MBM tracking algorithm demonstrates more accurate and

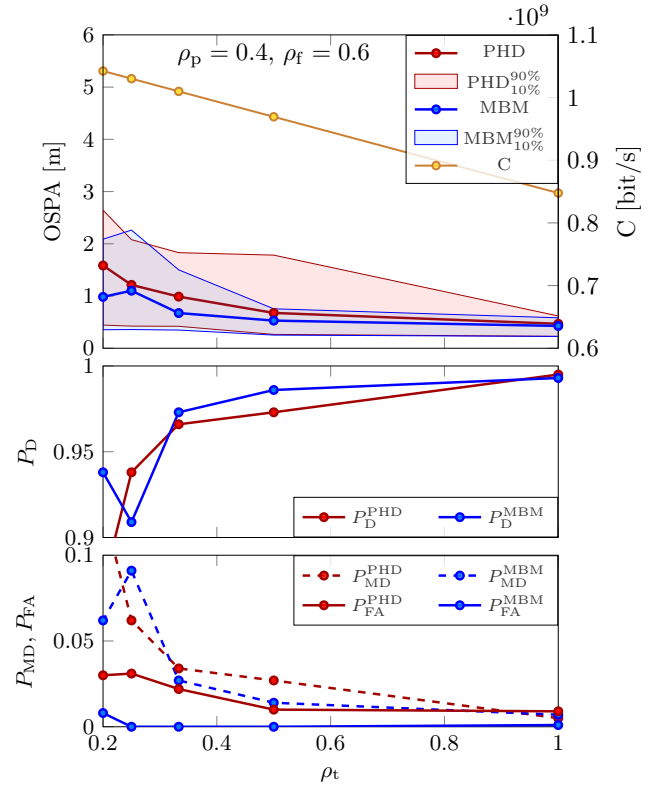


Figure 10. Communication and sensing performance varying the fraction of time reserved for JSC ρ_t . The downlink capacity is per BS.

stable performance compared to the PHD filter. This advantage arises from the MBM tracking algorithm's enhanced capability to handle missing measurements due to less frequent map acquisition.

Additionally, as the fraction of time allocated for JSC, ρ_t , increases, there is a decrease in the downlink sum rate. This decrease results from a lower fraction of time when all communication resources are available, limiting the overall downlink capacity. With ρ_t fixed at 0.5, the OSPA metric is around 0.5 m, while the downlink capacity is 0.97 Gbit/s. Halving ρ_t , the capacity increases to 1.03 Gbit/s, with a gain of 6%, while the localization performance decreases, with an OSPA distance around 1.2 m.

F. Sharing Threshold γ_s and Network Overhead

To investigate the impact of cooperation on both communication and sensing functionalities, in this section, we analyze their performance by varying the sharing threshold γ_s . The resources allocated for sensing are $\rho_p = 0.4$, $\rho_t = 0.6$, and $\rho_f = 0.5$. Remarkably, cooperative sensing with this resource configuration enables achieving localization errors below 0.8 m and a BS downlink capacity exceeding 1 Gbit/s.

As shown in Fig. 11, increasing the sharing threshold γ_s leads to a rapid decrease in the amount of data that BSs need to transfer to the FC compared to sharing the entire maps (i.e., $\gamma_s = 0$). Notably, when $\gamma_s < 0.1 \cdot 10^{-6} \text{ V}^2/\text{Hz}$, the data rate increases abruptly because most of the noise samples in the range-angle maps are shared with the FC.

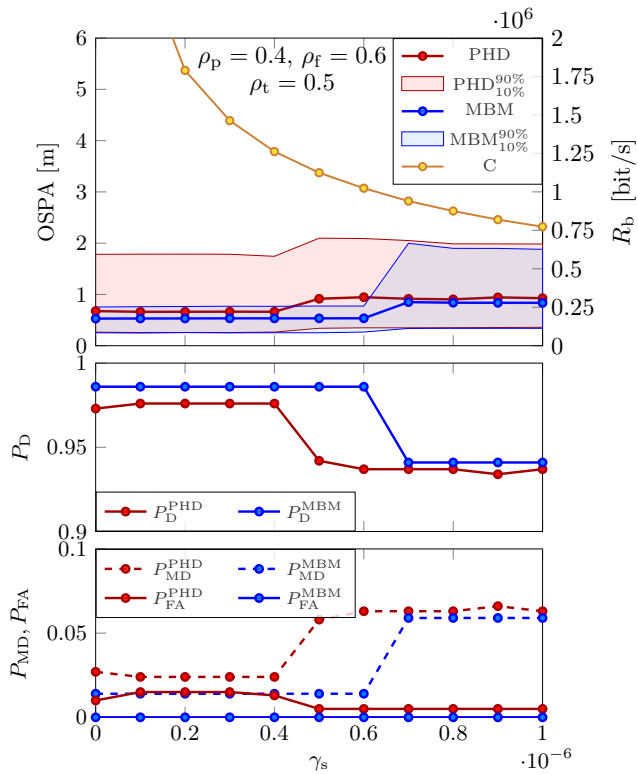


Figure 11. Network overhead due to cooperation and sensing performance varying the sharing threshold γ_s . The data rate is per BS.

By choosing an appropriate sharing threshold, a significant reduction in overhead is achieved, resulting in a required data rate $R_b = 613$ Kbit/s to share the selected map points compared to $R_b = 120$ Mbit/s when sharing the entire maps.

From the sensing perspective, increasing γ_s maintains stable system performance until the number of points filtered by the threshold becomes excessively high. In such situations, weak targets may go undetected, leading to an increase in the OSPA metric. Furthermore, in this setup, the MBM filter shows greater robustness to the lack of data caused by thresholding compared to PHD tracking. This characteristic allows for setting a larger threshold γ_s with benefits in terms of cooperation overhead.

G. Impact of Number of Sensors N_s

Communication and sensing performance, varying the number of BSs dedicated to sensing, are presented in Fig. 12, considering $\rho_p = 0.4$, $\rho_f = 0.6$, $\rho_t = 0.5$, and $\gamma_s = 0.4 \cdot 10^{-6}$ V²/Hz.

From a sensing perspective, it is important to note the increase in the OSPA error as the number of sensors N_s decreases. Moreover, the minimum number of sensors required to guarantee a localization error lower than 1 m is 3, and for a lower number of sensors, the error rapidly increases along with the detection probability. PHD and MBM exhibit comparable performance varying the number of sensors.

From a communication point of view, decreasing N_s slightly increases the downlink capacity. This increase is due to an

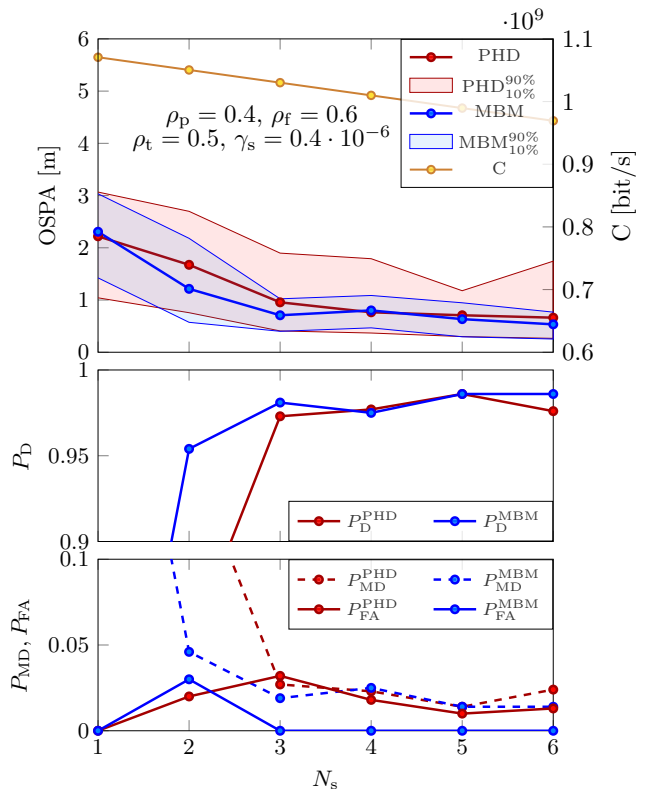


Figure 12. Communication and sensing performance varying the number of BSs adopted for sensing N_s . The downlink capacity is per BS.

increment of the communication resources that arise from BSs not selected to perform sensing.

V. CONCLUSION

In this work, we presented a JSC framework for OFDM systems, leveraging the infrastructure of mobile radio networks to enable cooperative sensing among BSs. We proposed a strategy to fuse soft maps acquired from BSs at a FC, along with a thresholding method for managing the amount of data shared between BSs and the FC. Two tracking algorithms, PHD and MBM filters, were employed, combined with a tailor-made three-step clustering strategy to address point-like and extended targets, specifically pedestrians and cars.

The overall networked system was tested by varying the fraction of resources allocated for sensing, including power (ρ_p), frequency (ρ_f), and time (ρ_t), while also considering network overhead managed through map thresholding. Localization performance was assessed through the OSPA metric, as well as the probability of detection and false alarm, while communication performance was evaluated through BS downlink sum rate.

Numerical results have shown that through the cooperation between BSs, the localization of both extended and point-like targets is possible with an error of less than 80 cm, while ensuring a downlink capacity greater than 1 Gbit/s, considering $\rho_p = 0.4$, $\rho_f = 0.6$, and $\rho_t = 0.5$. Through map management, the aforementioned results can be obtained with a network overhead of 613 kbit/s, reducing the amount of data shared

among BSs by a factor of 190 compared to 120 Mbit/s without any map filtering.

REFERENCES

- [1] S. Bartoletti, Z. Liu, M. Z. Win, and A. Conti, "Device-free localization of multiple targets in cluttered environments," *IEEE Trans. Aerosp. Electron. Syst.*, vol. 58, no. 5, pp. 3906–3923, Oct. 2022.
- [2] R. Thomä, T. Dallmann, S. Jovanoska, P. Knott, and A. Schmeink, "Joint communication and radar sensing: An overview," in *Proc. Europ. Conf. on Ant. and Prop. (EuCAP)*, Dusseldorf, Germany, Mar. 2021, pp. 1–5.
- [3] S. Schieler, C. Schneider, C. Andrich, M. Döbereiner, J. Luo, A. Schwind, R. S. Thomä, and G. Del Galdo, "OFDM waveform for distributed radar sensing in automotive scenarios," *Int. J. of Microw. and Wireless Tech.*, vol. 12, no. 8, p. 716–722, 2020.
- [4] G. Kwon, Z. Liu, A. Conti, H. Park, and M. Z. Win, "Integrated localization and communication for efficient millimeter wave networks," *IEEE J. Sel. Areas Commun.*, vol. 41, no. 12, Dec. 2023.
- [5] F. Morselli, S. M. Razavi, M. Z. Win, and A. Conti, "Soft information based localization for 5G networks and beyond," *IEEE Trans. Wireless Commun.*, vol. 22, pp. 1–16, 2023.
- [6] Z. Feng, Z. Wei, X. Chen, H. Yang, Q. Zhang, and P. Zhang, "Joint communication, sensing, and computation enabled 6G intelligent machine system," *IEEE Netw.*, vol. 35, no. 6, pp. 34–42, 2021.
- [7] J. Johnston, L. Venturino, E. Grossi, M. Lops, and X. Wang, "MIMO OFDM dual-function radar-communication under error rate and beam-pattern constraints," vol. 40, no. 6, pp. 1951–1964, 2022.
- [8] Y. Cui, F. Liu, X. Jing, and J. Mu, "Integrating sensing and communications for ubiquitous IoT: Applications, trends, and challenges," *IEEE Netw.*, vol. 35, pp. 158–167, 2021.
- [9] F. Liu, P. Zhao, and Z. Wang, "EKF-based beam tracking for mmWave MIMO systems," *IEEE Commun. Lett.*, vol. 23, no. 12, pp. 2390–2393, 2019.
- [10] Z. Du, F. Liu, and Z. Zhang, "Sensing-assisted beam tracking in V2I networks: Extended target case," in *Proc. IEEE Int. Conf. on Acoustics, Speech and Signal Process. (ICASSP)*, May 2022, pp. 8727–8731.
- [11] E. Favarelli, E. Matricardi, L. Pucci, E. Paolini, W. Xu, and A. Giorgetti, "Map fusion and heterogeneous objects tracking in joint sensing and communication networks," in *Proc. European Radar Conf. (EuRAD)*, Berlin, Germany, Sep. 2023.
- [12] —, "Sensor fusion and extended multi-target tracking in joint sensing and communication networks," in *Proc. IEEE Int. Conf. on Commun. (ICC)*, Rome, Italy, May 2023.
- [13] —, "Multi-base station cooperative sensing with ai-aided tracking," in *arXiv*, Oct. 2023.
- [14] L. Pucci, E. Paolini, and A. Giorgetti, "System-level analysis of joint sensing and communication based on 5G new radio," in *IEEE J. Sel. Areas Commun.*, vol. 40, no. 7, July 2022, pp. 2043–2055.
- [15] H. Asplund, D. Astely, P. von Butovitsch, T. Chapman, M. Frenne, F. Ghasemzadeh, M. Hagström, B. Hogan, G. Jöngren, J. Karlsson *et al.*, *Advanced Antenna Systems for 5G Network Deployments: Bridging the Gap Between Theory and Practice*. Academic Press, 2020.
- [16] E. Favarelli, E. Matricardi, L. Pucci, E. Paolini, W. Xu, and A. Giorgetti, "Tracking and data fusion in joint sensing and communication networks," in *Proc. IEEE Globecom Workshops*, Rio de Janeiro, Brasil, Dec. 2022, pp. 341–346.
- [17] M. A. Richards, *Fundamentals of radar signal processing*. McGraw-Hill, 2005.
- [18] M. F. Keskin, V. Koivunen, and H. Wymeersch, "Limited feedforward waveform design for OFDM dual-functional radar-communications," *IEEE Trans. Signal Process.*, vol. 69, pp. 2955–2970, 2021.
- [19] M. F. Keskin, H. Wymeersch, and V. Koivunen, "MIMO-OFDM joint radar-communications: Is it friend or foe?" *IEEE J. Sel. Topics in Signal Process.*, vol. 15, no. 6, pp. 1393–1408, 2021.
- [20] M. Alhassoun and G. D. Durgin, "A theoretical channel model for spatial fading in retrodirective backscatter channels," *IEEE Trans. Wireless Commun.*, vol. 18, no. 12, pp. 5845–5854, 2019.
- [21] S. D. Blunt, J. G. Metcalf, C. R. Biggs, and E. Perrins, "Performance characteristics and metrics for intra-pulse radar-embedded communication," *IEEE J. Sel. Areas Commun.*, vol. 29, no. 10, pp. 2057–2066, 2011.
- [22] M. I. Skolnik, *Radar handbook*. McGraw-Hill Education, 2008.
- [23] M. Bühren and B. Yang, "Automotive radar target list simulation based on reflection center representation of objects?" in *Proc. Int. Work. on Intelligent Transp. (WIT)*, Hamburg, Germany, Mar. 2006, pp. 161–166.
- [24] —, "Simulation of automotive radar target lists using a novel approach of object representation," in *Proc. IEEE Intelligent Veh. Symp.*, Meguro-Ku, Japan, 2006, pp. 314–319.
- [25] M. Braun, "OFDM radar algorithms in mobile communication networks," Ph.D. dissertation, Karlsruhe Institute of Technology, 2014.
- [26] J. T. Rodriguez, G. P. Blasone, F. Colone, and P. Lombardo, "Exploiting the properties of reciprocal filter in low-complexity OFDM radar signal processing architectures," *IEEE Trans. Aerosp. Electron. Syst.*, vol. 59, no. 5, pp. 6907–6922, 2023.
- [27] C. B. Barneto, T. Riihonen, M. Turunen, L. Anttila, M. Fleischer, K. Stadius, J. Ryyänen, and M. Valkama, "Full-duplex OFDM radar with LTE and 5G NR waveforms: challenges, solutions, and measurements," *IEEE Trans. Microw. Theory Tech.*, vol. 67, no. 10, pp. 4042–4054, 2019.
- [28] M. Henninger, S. Mandelli, M. Arnold, and X. Ten Brink, "A computationally efficient 2D MUSIC approach for 5G and 6G sensing networks," in *Proc. IEEE Wireless Comm. and Netw. Conf. (WCNC)*, Austin, TX, USA, Apr. 2022, pp. 210–215.
- [29] Y. Xiong, F. Liu, Y. Cui, W. Yuan, T. X. Han, and G. Caire, "On the fundamental tradeoff of integrated sensing and communications under Gaussian channels," *IEEE Trans. Inf. Theory*, vol. 69, no. 9, pp. 5723–5751, 2023.
- [30] H. Y. Chongjun Ouyang, Sheng Wu, "Mutual information approximation," *arXiv*, 2019.
- [31] J. Watt, R. Borhani, and A. K. Katsaggelos, *Machine Learning Refined*. Cambridge University Press, 2016.
- [32] M. Ester, H.-P. Kriegel, J. Sander, and X. Xu, "A density-based algorithm for discovering clusters in large spatial databases with noise," in *Proc. Int. Conf. on Know. Disc. in Data Mining*, Portland, Oregon, Aug. 1996, pp. 226–231.
- [33] R. Mahler, "Multitarget Bayes filtering via first-order multitarget moments," *IEEE Trans. Aerosp. Electron. Syst.*, vol. 39, no. 4, pp. 1152–1178, 2003.
- [34] B.-N. Vo and W.-K. Ma, "The gaussian mixture probability hypothesis density filter," *IEEE Trans. Signal Process.*, vol. 54, no. 11, pp. 4091–4104, 2006.
- [35] A. F. García-Fernández, Y. Xia, K. Granström, L. Svensson, and J. L. Williams, "Gaussian implementation of the multi-bernoulli mixture filter," in *Proc. Int. Conf. on Inf. Fusion (FUSION)*, Ottawa, Canada, 2019, pp. 1–8.
- [36] A. F. García-Fernández, J. L. Williams, K. Granström, and L. Svensson, "Poisson multi-bernoulli mixture filter: Direct derivation and implementation," *IEEE Trans. Aerosp. Electron. Syst.*, vol. 54, no. 4, pp. 1883–1901, 2018.
- [37] L. B. Thanh, P. D. Alexandrovich, and P. Ruben, "Multi-object multi-sensor tracking simulation using poisson multi-bernoulli mixture filter," in *Proc. Int. Conf. on Digital Signal Process. and its Applications (DSPA)*, Moscow, Russian Federation, 2021, pp. 1–6.
- [38] D. Schuhmacher, B.-T. Vo, and B.-N. Vo, "A consistent metric for performance evaluation of multi-object filters," *IEEE Trans. Signal Process.*, vol. 56, no. 8, pp. 3447–3457, Aug. 2008.
- [39] M. Beard, B. T. Vo, and B.-N. Vo, "OSPA(2): Using the OSPA metric to evaluate multi-target tracking performance," in *Proc. Int. Conf. on Control, Autom. and Inf. Sci. (CCAIS)*, Chiang Mai, Thailand, 2017, pp. 86–91.
- [40] A. S. Rahmattullah, A. F. García-Fernández, and L. Svensson, "Generalized optimal sub-pattern assignment metric," in *Proc. Int. Conf. on Inf. Fusion (FUSION)*, Xi'an, China, 2017, pp. 1–8.
- [41] *Study on channel model for frequencies from 0.5 to 100 GHz*, 3GPP TR 38.901, 2019, version 16.1.0.
- [42] S. Jaeckel, L. Raschkowski, K. Börner, and L. Thiele, "Quadriga: A 3-d multi-cell channel model with time evolution for enabling virtual field trials," *IEEE Trans. Antennas Propag.*, vol. 62, no. 6, pp. 3242–3256, 2014.